Journal of The Electrochemical Society, **146** (9) 3217-3223 (1999)
S0013-4651(99)01-103-9 CCC: $7.00 © The Electrochemical Society, Inc.

Electrochemical Cycling-Induced Spinel Formation in High-Charge-Capacity Orthorhombic $LiMnO_2$

Young-Il Jang,* Biying Huang, Haifeng Wang,** Donald R. Sadoway,** and Yet-Ming Chiang**,z**

Department of Materials Science and Engineering, Massachusetts Institute of Technology, Massachuesetts 02139, USA

$Li_xMn_2O_4$ spinel normally undergoes a transformation from its cubic to tetragonal phase when x exceeds 1 due to a collective Jahn-Teller distortion, resulting in poor cyclability when both the 4 and 3 V intercalation plateaus are utilized. In this study, we show that this transformation is suppressed in spinels of composition up to $x \approx 2$ obtained through the electrochemical cycling of orthorhombic $LiMnO_2$. X-ray diffraction, transmission electron microscopy, and high-resolution electron microscopy studies together show that cycling produces a cubic spinel containing partial tetrahedral cation site occupancy and a nanodomain structure (20 to 50 nm size) within parent single-crystalline oxide particles. This structure is responsible for the cycling stability of electrochemically produced spinel. The reversible capacity (272 mAh/g) and energy density (853 Wh/kg) achieved at a low charge-discharge rate (3.33 mA/g) in the present samples are the highest among crystalline $LiMnO_2$ materials reported to date.

Manuscript submitted January 29, 1999; revised manuscript received April 8, 1999.

Due to its low cost and nontoxicity, $LiMn_2O_4$ spinel has attracted wide attention as an intercalation cathode for rechargeable lithium batteries.[1-3] This phase is usually used within its 4 V plateau (the voltage being with respect to Li metal), since it shows significant capacity fade when cycled over both the 4 and 3 V plateaus.[1,2] The onset of a collective Jahn-Teller distortion and the consequent structural instability that occurs when $Li_xMn_2O_4$ is discharged to an average Mn valence < 3.5 (*i.e.*, when $x > 1$) is generally believed to be responsible for the rapid capacity loss when discharge reaches the 3 V plateau.[4,5] Even when $LiMn_2O_4$ is cycled over only the 4 V plateau, a slow capacity fade is usually observed.[6,7] Efforts have been made to improve the cyclability by suppressing the Jahn-Teller distortion by replacing Mn by other ions, *e.g.*, Li, Zn, Mg, etc.[6]

Orthorhombic $LiMnO_2$ (space group *Pmnm*, hereafter referred to as *o*-$LiMnO_2$) shows better cyclability than $LiMn_2O_4$ when both the 4 and 3 V plateaus are utilized.[8-16] X-ray diffraction (XRD) studies have verified an irreversible transformation to spinel-like structure during the first charge,[9-11,17] consistent with the appearance of two plateaus at ≈4 and ≈3 V upon cycling. However, the mechanism by which the cyclability of *o*-$LiMnO_2$ is improved remains to be elucidated. XRD studies by Gummow *et al.*[10,11] showed that the transformed material is a cubic spinel in the partially discharged state ($Li_{0.4}MnO_2$). This is not surprising since at that concentration ($x < 1$) the spinel is expected to be cubic. Croguennec *et al.*[16] conducted XRD studies on *o*-$LiMnO_2$ discharged onto the 3 V plateau, with capacities of 130 to 165 mAh/g, and also observed a cubic spinel. This shows that the cubic phase can be retained to a Li concentration $x > 1$. At the observed capacities, full lithiation has not yet been reached, since the theoretical capacity is 285 mAh/g, assuming lithiation to a limiting composition of $LiMnO_2$.

Previous studies have also suggested that low-temperature synthesis is necessary to obtain a high capacity in *o*-$LiMnO_2$.[10] Croguennec *et al.*[14,16,18,19] proposed that the electrochemical performance of *o*-$LiMnO_2$ is improved by structural disorder between Li and Mn sites occurring in the form of monoclinic stacking faults (local regions of monoclinic order). The density of these faults was increased by low-temperature synthesis. Nonetheless, significant capacity fade is reported upon cycling over both the 4 and 3 V plateaus in low-temperature prepared *o*-$LiMnO_2$, although it is less severe than in $Li_xMn_2O_4$ spinels. *o*-$LiMnO_2$ synthesized at 300 to 450°C using γ-MnOOH as a precursor was reported to have a capacity of 60 to 190 mAh/g during the first few cycles and capacity loss of 8 mAh/g per cycle at a current rate of 5.7 mA/g.[9] Koetschau *et al.*[12] reported that *o*-$LiMnO_2$ obtained at 100°C has a substantially worse cyclability when cycled over both the 4 and 3 V plateaus than over only one plateau, losing capacity on the 3 V plateau upon cycling.[12,17] Shu *et al.*[15] reported that *o*-$LiMnO_2$ fired at 800 to 1000°C has an initial discharge capacity of 199 to 257 mAh/g between 1.0 and 4.4 V (1.78 to 3.56 mA/g rates), but did not show the subsequent cycling performance.

This paper reports on two advances with respect to *o*-$LiMnO_2$. First, contrary to conventional wisdom, we show that a highly ordered material prepared by a new high-temperature synthesis route yields excellent cyclability over both the 4 and 3 V plateaus. Second, by being able to achieve near-theoretical values of discharge capacity at low current densities (>95% of the theoretical limit based on Mn valence), we were able to study the structure of samples that are essentially completely lithiated ($x \approx 2$). Using transmission electron microscopy (TEM) and high-resolution electron microscopy (HREM) to observe directly the structure of the cycled oxides, we show for the first time that a unique, nanodomain structure is produced by the cycling-induced phase transformation. A model is presented that explains why a spinel produced by an electrochemical transformation is able to intercalate Li reversibly in the Jahn-Teller regime whereas a high-temperature annealed spinel is not.

Experimental

Mn_3O_4 and $LiOH \cdot H_2O$ (Alfa Aesar, 98%) were used as starting materials in this study. Mn_3O_4 was prepared by a precipitation method[20] and dispersed with LiOH by a freeze-drying technique as detailed elsewhere.[21] The precursor powders were fired for 12 h at $T = 950$°C, $p_{O_2} = 10^{-6}$ atm. Oxygen partial pressure was controlled by flowing an argon/oxygen mixture. The oxide powders were characterized by TEM (200 kV JEOL 2000FX), HREM (200 kV Topcon 002B using double tilt sample holder), and XRD (Rigaku RTP500RC using Cu Kα radiation).

For electrochemical testing, cathodes were prepared by mixing the oxide powders, carbon black (Cabot), graphite (TIMCAL America), and poly(vinylidene fluoride) (PVDF) (Aldrich) in the weight ratio of 70:15:5:10 using a procedure described elsewhere.[22] Components were compacted at 4 t/cm^2 pressure to form cathode pellets 15 to 20 mg in weight (weighed to <0.1 mg precision), 0.3 mm in thickness, and 1 cm^2 in cross-sectional area. Lithium ribbon of 0.75 mm thickness (Aldrich) was used as the anode. The separator was a film of Celgard 2400™. The electrolyte consisted of a 1 M solution of $LiPF_6$ in a 1:1 mixture (by volume) of ethylene carbonate (EC) and diethyl carbonate (DEC). All cell handling was performed in an argon-filled glove box. Charge-discharge studies were performed with Maccor automated test equipment (Series 4000). All electrochemical testing was conducted at room temperature.

* Electrochemical Society Student Member.
** Electrochemical Society Active Member.
z E-mail: YCHIANG@MIT.EDU

S0013-4651(99)01-103-9 CCC: $7.00

Cyclic voltammetry studies were carried out in a three-electrode cell with a Solartron 1286 potentiostat controlled by CorrWare running on a PC. Cyclic voltammograms were taken at a scan rate of 0.02 mV/s over the potential range in which no electrolytic decomposition occurs. An *o*-$LiMnO_2$ working electrode, 0.2 cm^2 in cross-sectional area, was prepared. Lithium foil was used as the counter electrode with a cross-sectional area of 2 cm^2, and lithium wire was used as the reference electrode.

After electrochemical cycling, XRD and TEM/HREM studies were performed on a composite cathode pellet that exhibited nearly the theoretical capacity upon discharge. The sample was examined at the end of discharge. In order to minimize exposure to moisture in air, the cell was disassembled in a glove box, and the electrode was hermetically sealed with a covering of tape through which XRD could be performed. Pieces of the cathode were ultrasonically deagglomerated and dispersed on an amorphous carbon film for TEM/HREM observation as described in Ref. 23.

Results and Discussion

The XRD pattern of the oxide powder after firing for 12 h at T = 950°C, $p_{O_2} = 10^{-6}$ atm is shown in Fig. 1. *o*-$LiMnO_2$ was obtained as the predominant phase with Li_2MnO_3 as a minor phase. The *hkl* indexes indicated correspond to the space group *Pmnm*. It is notable that the full width at half maximum (fwhm) of the (011) peak at 2θ = 24.8° is 0.15°. Croguennec *et al.*[19] correlated the width of this peak with the density of monoclinic stacking faults occurring in *o*-$LiMnO_2$. They obtained a capacity of 45 to 78 mAh/g from samples with 1% stacking faults at a C/15 current rate (corresponding to 3 to 5.2 mA/g based on the 20th discharge capacities reported in Ref. 16), and 130 to 165 mAh/g from samples with 3% stacking faults (8.7 to 11 mA/g). Based on these results, they suggested that synthesis conditions should be directed toward creating the defective structure in order to obtain improved electrochemical performance. However, the width of 0.15° in Fig. 1 corresponds to ≈1% stacking faults according to their analysis,[19] indicating that the present material in this study has a well-ordered orthorhombic structure and should not show high capacity. The average particle size of the present material was determined to be ≈1 μm by TEM as shown in Fig. 2.

Figures 3 and 4 show the first charge-discharge curve and corresponding differential capacity plot, measured between 2.0 and 4.4 V at 45.9 mA/g rate. The cell exhibits a single charging voltage plateau at 3.65 V, and has 147 mAh/g of first charge capacity, while the first discharge capacity is 42 mAh/g. The large capacity loss during the first cycle has been observed previously; Shu *et al.*[15] showed first-cycle capacity loss of 70 mAh/g at 0.7 mA/g rate and reported that the capacity loss increases as the charge-discharge rate increases. Figures 3 and 4 show that while Li is removed from *o*-$LiMnO_2$ over a plateau at 3.65 V during the first charge, Li insertion occurs mainly below 3.0 V during the first discharge, indicating that a structural transformation occurs during the first cycle.

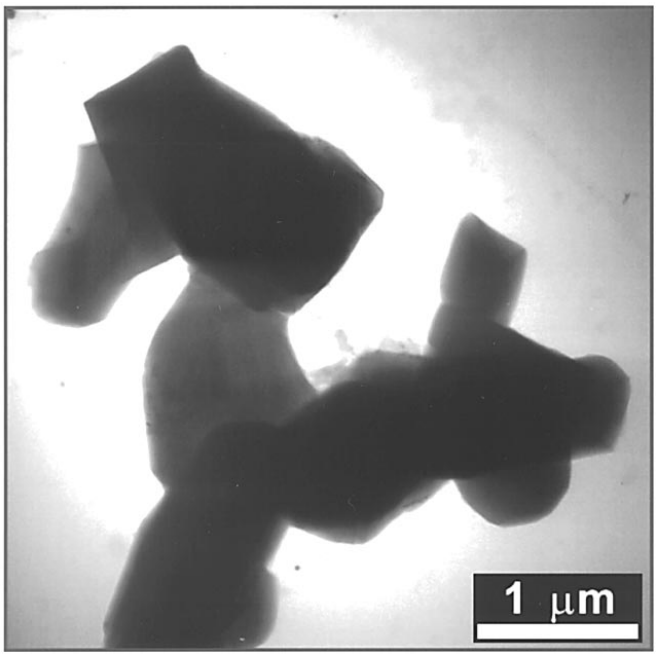

Figure 2. TEM micrograph of *o*-$LiMnO_2$ particles obtained after firing for 12 h at T = 945°C, $p_{O_2} = 10^{-6}$ atm.

With further cycling, voltage plateaus develop at ≈4 and ≈2.9 V, respectively, as shown in Fig. 5 and 6, indicative of Li intercalation on two different sites. This behavior is characteristic of the spinel phase $Li_xMn_2O_4$, in which Li is inserted into tetrahedral sites over the 4 V plateau corresponding to $0 < x \leq 1$, and into the octahedral sites over the 3 V plateau corresponding to $1 < x \leq 2$.[24] Notice that the 4 V plateau shows a two-step profile at 4.05 and 4.2 V during the charge and at 3.95 and 4.05 V during discharge. This is also observed in conventionally prepared $Li_xMn_2O_4$ spinel.[24,25] An additional differential capacity peak is seen at 3.8 V during charging, which has previously seen in $LiMn_2O_4$ and $Li_2Mn_2O_4$ cycled over both 4 and 3 V plateaus, although its origin is unknown.[26] These results support previous reports that *o*-$LiMnO_2$ transforms to spinel-like cation ordering during electrochemical cycling.[8-17] It is also noteworthy that the 3 V plateau exhibits larger apparent polarization

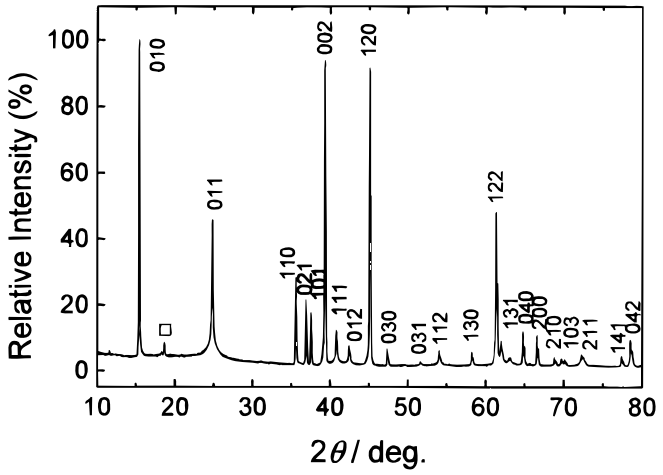

Figure 1. Powder X-ray diffraction patterns of *o*-$LiMnO_2$, with *hkl* indicated, obtained after firing for 12 h at T = 945°C, $p_{O_2} = 10^{-6}$ atm, (□: Li_2MnO_3).

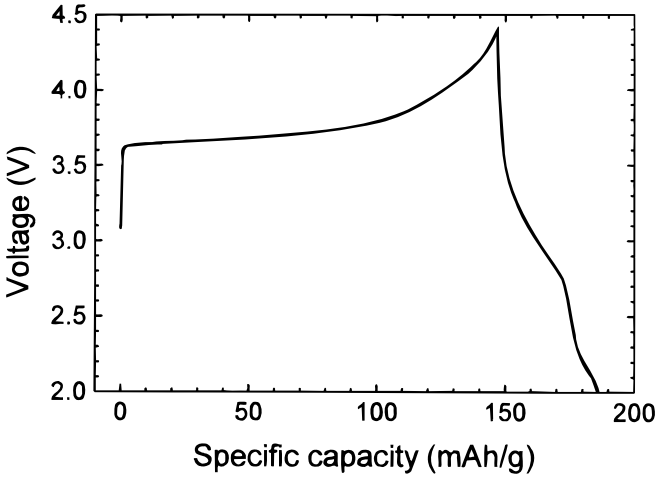

Figure 3. First charge-discharge curve for *o*-$LiMnO_2$ tested against a Li metal anode at 45.9 mA/g rate between 2.0 and 4.4 V.

S0013-4651(99)01-103-9 CCC: $7.00

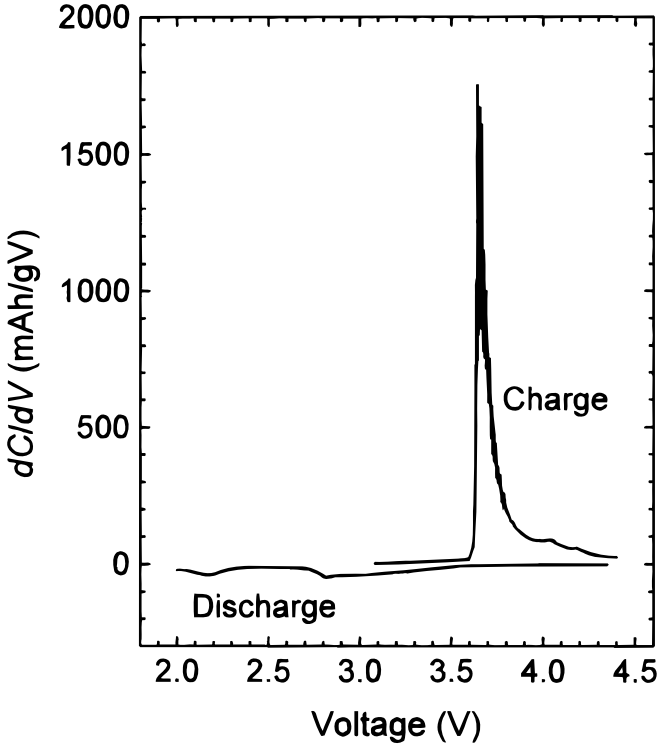

Figure 4. Differential capacity plots for the first charge-discharge cycle for *o*-$LiMnO_2$ tested against a Li metal anode at 45.9 mA/g rate between 2.0 and 4.4 V. *C* and *V* represent the capacity and voltage, respectively.

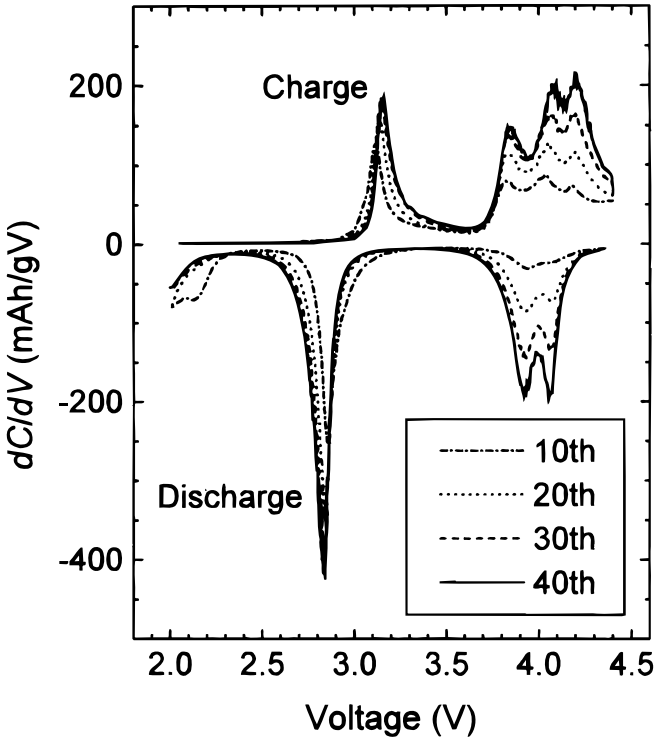

Figure 6. Evolution of differential capacity plots upon cycling for *o*-$LiMnO_2$ tested against a Li metal anode at 45.9 mA/g rate between 2.0 and 4.4 V. Results are shown for the 10th, 20th, 30th, and 40th cycles. *C* and *V* represent the capacity and voltage, respectively.

than the 4 V plateau, seen by the differences in voltage of the differential capacity peaks in Fig. 6.

An additional capacity of ≈15 mAh/g is seen below 2.5 V in the 10th discharge curve of Fig. 5. The cyclic voltammogram in Fig. 7 clearly shows a reduction peak at ≈2 V, but this peak does not appear during oxidation. Interestingly, this additional capacity decreases with further cycling. It is possibly due to the formation of a Li-rich metastable phase. Formation of Li_2MnO_2 in *o*-$LiMnO_2$ has been suggested previously,[15] and is observed in $Li_xMn_2O_4$ ($2 < x \leq 4$).[24,27] Note that the 2 V plateau is not correlated with high lithiation, since it occurs even when the delivered discharge capacity is only 70 mAh/g. If it is due to a highly lithiated metastable phase, the phase appears to form nonuniformly within the cathode. Previous TEM observations have shown that inhomogeneous reactions occur in typically formulated $LiCoO_2$ electrodes,[23] even within single oxide particles.

Figure 8 shows the evolution of the charge and discharge capacities during cycling between 2.0 and 4.4 V at 45.9 mA/g. It is seen that the present material can be cycled over both the 4 and 3 V plateaus without significant capacity fade for >130 cycles, which is a remarkably different behavior from that of $Li_xMn_2O_4$ spinels, in which the capacity decreases sharply with a few cycles into the 3 V region.[1,2] While an initial drop in capacity to 36 mAh/g is observed over the first two cycles, the capacities increase progressively with further cycling and saturate after 40 cycles at ≈130 mAh/g. We attribute the progressive increase in capacity that occurs during the

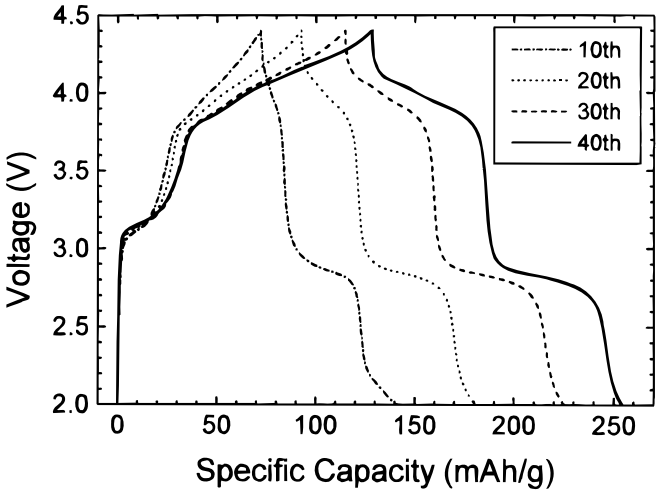

Figure 5. Evolution of charge-discharge curves upon cycling for *o*-$LiMnO_2$ tested against a Li metal anode at 45.9 mA/g rate between 2.0 and 4.4 V. Voltage profiles are shown for the 10th, 20th, 30th, and 40th cycles.

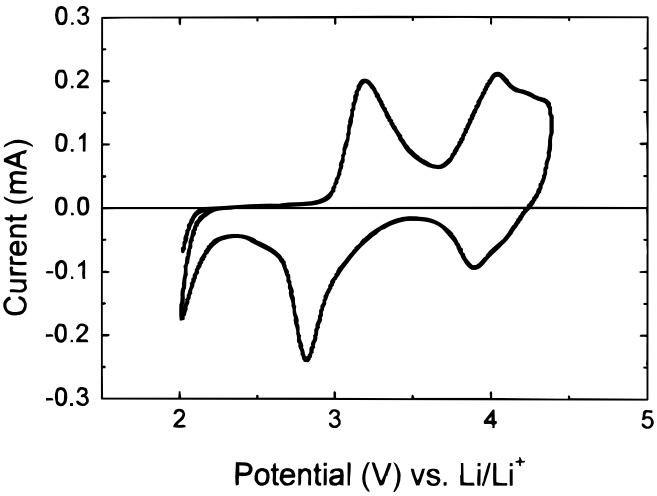

Figure 7. Cyclic voltammogram of *o*-$LiMnO_2$ at 0.02 mV/s scanning rate between 2.0 and 4.4 V. The data were obtained after three cycles.

S0013-4651(99)01-103-9 CCC: $7.00

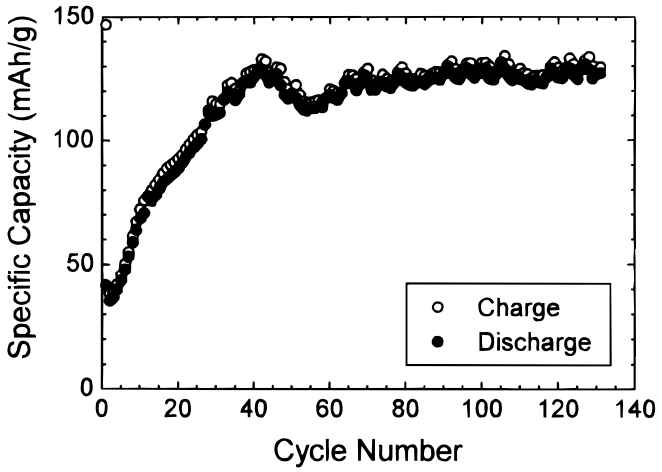

Figure 8. Specific capacity *vs*. cycle number for *o*-$LiMnO_2$ tested against a Li metal anode at 45.9 mA/g rate between 2.0 and 4.4 V.

initial 40 cycles to the establishment of an increasingly ordered spinel upon cycling. As discussed by Gummow *et al.*[10] and Tang *et al.*,[28] the transformation of *o*-$LiMnO_2$ to spinel structure requires displacement of 50% of the Mn ions to octahedral sites vacated by extraction of the Li ions, via neighboring tetrahedral sites within the cubic close-packed oxygen sublattice. During the initial transient in capacity it is likely that the cation ordering has not yet reached that of the $LiMn_2O_4$ spinel structure; the ordering may be partly that of an inverse spinel.

This interpretation is supported by an examination of the evolution of capacity on the two voltage plateaus with cycling. We separated the discharge capacity into a 4 V plateau capacity (between 3.4 and 4.4 V) and a 3 V plateau capacity (between 2.3 and 3.4 V) as shown in Fig. 9. These voltage limits correspond to minimum values of the differential capacity ($|dC/dV|$) during discharge (Fig. 6) and clearly separate the voltage plateaus. The ratio of 3 V capacity to 4 V capacity is plotted in Fig. 10. Note that the 3 V capacity is higher than the 4 V capacity during the initial 40 cycles (Fig. 9), indicating that Li ions are preferentially inserted into the octahedral sites over the tetrahedral sites. Limited insertion of the Li ions into the tetrahedral sites is consistent with partial occupation of these sites by Mn ions. If upon further cycling the Mn ions are increasingly ordered on the spinel octahedral sites (16*d*), the 3 V capacity should then decrease relative to the 4 V capacity, which we observe (Fig. 10). Note that, after the total capacity has saturated, the 3 V capacity fades slowly (Fig. 9). Kötschau and Dahn also reported that cycled *o*-$LiMnO_2$ exhibits capacity fade primarily on the 3 V plateau.[17] The capacity loss rate in the present material is significantly less than that of Ref. 17 (0.05 mAh/g per cycle *vs*. ≈1.4 mAh/g per cycle).

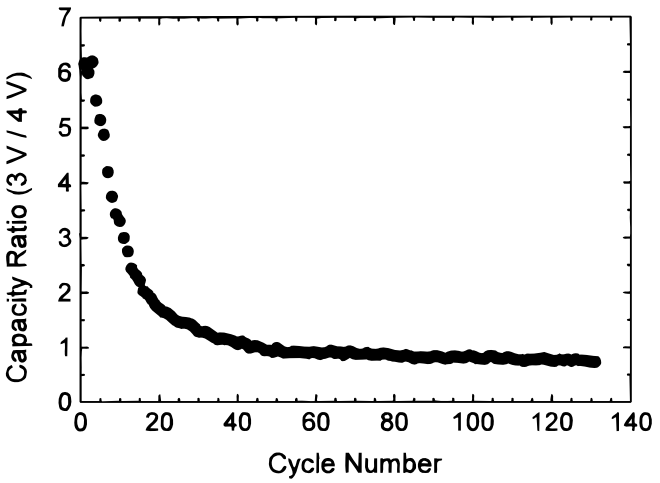

Figure 10. Ratio of 4 and 3 V plateau discharge capacities *vs*. cycle number for *o*-$LiMnO_2$ tested against a Li metal anode at 45.9 mA/g rate between 2.0 and 4.4 V. 4 and 3 V capacities were calculated in the voltage ranges of 3.4 to 4.4 and 2.3 to 3.4 V, respectively.

Charge-discharge tests were conducted at various current densities. A fresh cell was cycled 41 times at 33.3 mA/g rate, followed by two cycles at 8.33 mA/g and several cycles at 3.33 mA/g between 2.0 and 4.4 V. Figure 11 shows the discharge capacities thus obtained. At 33.3 mA/g rate, the capacity reaches a steady-state value of *ca*. 130 mAh/g after about 30 cycles. With decreasing current density, the capacity and energy density increase as shown in Fig. 11 and 12. At 3.33 mA/g, a discharge capacity of 272 mAh/g (95% of the theoretical capacity of $LiMnO_2$) and an energy density of 853 Wh/kg were obtained, which are the highest values reported to date in a crystalline Li-Mn-O system. A capacity of ≈30 mAh/g occurs below 2.5 V at the current rates of 8.33 and 3.33 mA/g. Figure 13 compares the differential capacity plots obtained at 33.3 and 8.33 mA/g rates. The polarization decreases as the current rate decreases, as is expected. Interestingly, the position of the oxidation peak marked A in Fig. 13 shows a greater voltage shift than the other peaks, decreas-

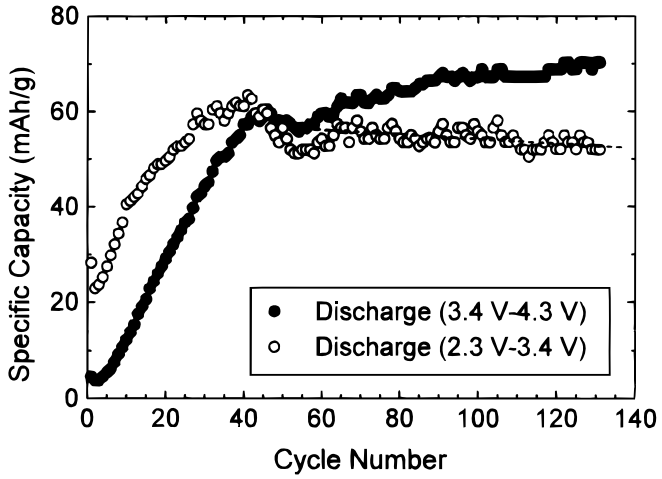

Figure 9. 4 and 3 V plateau discharge capacities *vs*. cycle number for *o*-$LiMnO_2$ tested against a Li metal anode at 45.9 mA/g rate between 2.0 and 4.4 V. 4 and 3 V capacities were calculated in the voltage ranges of 3.4 to 4.4 V and 2.3 to 3.4 V, respectively. Dashed line shows a capacity loss rate for the 3 V capacity of 0.05 mAh/g per cycle.

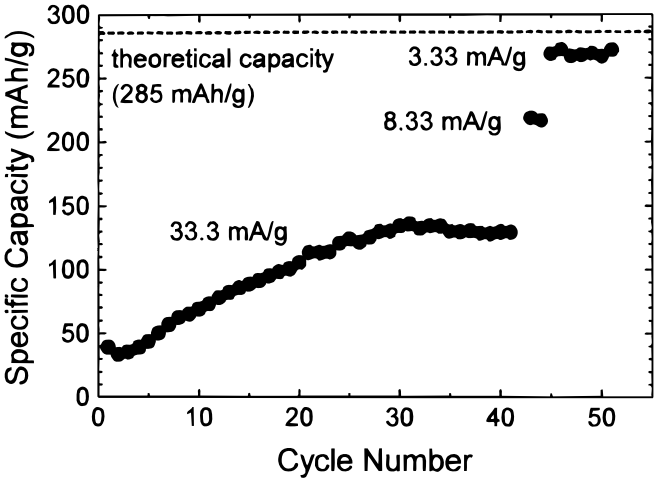

Figure 11. Specific capacity *vs*. cycle number for *o*-$LiMnO_2$ tested against a Li metal anode between 2.0 and 4.4 V at various cycling rates of 33.3, 8.33, and 3.33 mA/g.

S0013-4651(99)01-103-9 CCC: $7.00

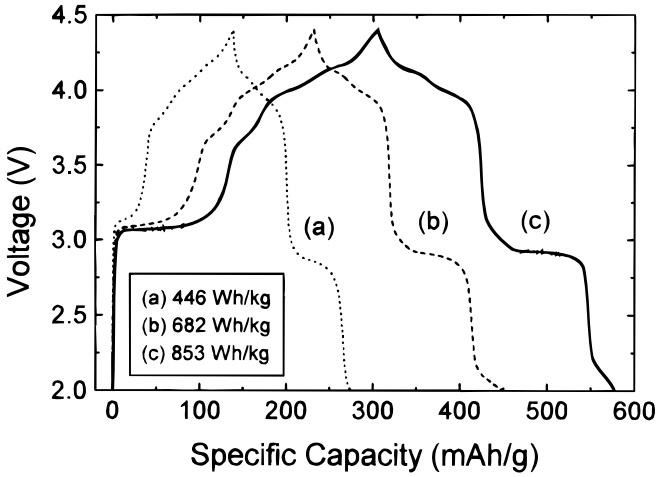

Figure 12. Charge-discharge curves for *o*-$LiMnO_2$ at (a) 33.3 mA/g (31st cycle), (b) 8.33 mA/g (44th cycle), and (c) 3.33 mA/g rates (46th cycle) between 2.0 and 4.4 V. The cell was first cycled 41 times at 33.3 mA/g; the 42nd and 43rd cycles were conducted at 8.33 mA/g, and the 44th cycle at 3.33 mA/g. The corresponding energy densities are indicated in the inset.

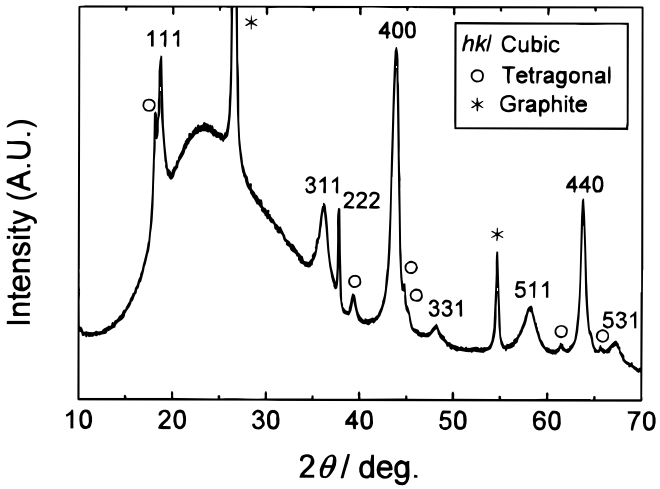

Figure 14. X-ray diffraction pattern of *o*-$LiMnO_2$ cathode after cycling 51 times between 2.0 and 4.4 V. The cell was first cycled 41 times at 33.3 mA/g; the 42nd and 43rd cycles were conducted at 8.33 mA/g. The last eight cycles were tested at 3.33 mA/g rate. Cubic spinel is indicated by *hkl*, while tetragonal spinel and graphite are indicated by ○ and ∗, respectively.

ing from 3.8 to 3.7 V as the current rate decreases from 33.3 to 8.33 mA/g. The origin of the peak and its current-density dependence are not yet understood.

Previous structural studies on cycled *o*-$LiMnO_2$ electrodes were limited to materials of lower capacity and higher cycling fade than the present samples.[10-12,16,17] We conducted X-ray diffraction on the composite cathode of the cell used in Fig. 11 after 51 cycles. For the last eight cycles, the cell was cycled at 3.33 mA/g rate between 2.0 and 4.4 V. Since in the charged state the Li concentration of the oxide cannot be less than zero, that is, the compound can at most be delithiated to a composition MnO_2, the measured discharge capacity indicates that the material was discharged to a composition $Li_xMn_2O_4$ where $x \geq 1.9$. That is, the overall composition is very nearly that of the tetragonal spinel $Li_2Mn_2O_4$. However, the strong diffraction peaks at $2\theta = 44°$ [indexed as (400)] and 64° [indexed as (440)] in Fig. 14, which are absent in the case of tetragonal spinel (space group $I4_1/amd$), clearly show that the major crystalline phase still has an overall cubic symmetry. The tetragonal spinel is present as a minority phase in Fig. 14, but Li_2MnO_2 [27] is not detected. The broad and high background at low angles is due to the amorphous components of the composite electrode and the sealing tape.

The XRD pattern shows very broad diffraction lines, which can be attributed to small crystallite size and/or lattice strain in the electrode oxide after cycling. The separation of size and strain broadening is possible because strain broadening scales with the reciprocal space variable s ($s = 2\sin\theta/\lambda$) while size broadening is independent of s.[29] When both size and strain broadening are present, it is necessary to make an assumption as to the shapes of the two contributing line profiles in order to quantify the individual contributions. We considered three models: Cauchy/Cauchy, Gaussian/Gaussian, and Cauchy/Gaussian for the size/strain broadening functions, respectively.[29] The results corresponding to each assumption are shown in Table I and are relatively insensitive to the assumed line profiles. From this analysis, the crystallite size is determined to be <50 nm, and the lattice strain on the order of 1%. Note that the original particles were ≈1 μm in size and appeared from XRD to be strain free before electrochemical cycling, as shown in Fig. 1 and 2. Clearly, the small crystallite size and strain developed during cycling.

In order to understand better the structure of the cycled oxide, we performed direct observations by TEM and HREM on the same electrode sample as was studied by XRD. Figure 15 shows a typical TEM image of the cycled particles and the corresponding selected area diffraction (SAD) pattern. Observation of 20 particles gave the same SAD pattern, indicating that Fig. 15 is representative of the major phase after cycling. This pattern shows a cubic spinel, consis-

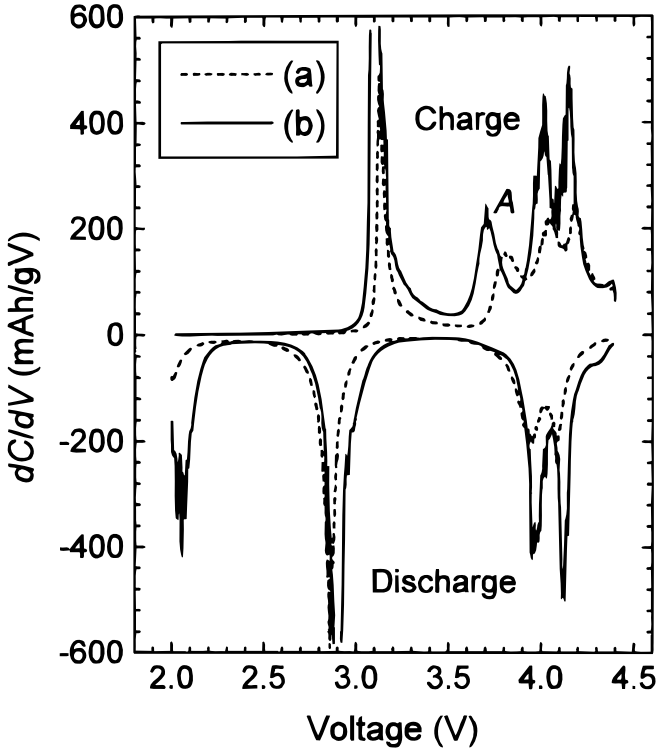

Figure 13. Differential capacity plots for *o*-$LiMnO_2$ at (a) 33.3 mA/g (31st cycle) and (b) 8.33 mA/g rates (44th cycle) between 2.0 and 4.4 V. See text for discussion of peak *A*.

Table I. Separation of size and strain broadening of X-ray diffraction lines in Fig. 14.

Size/strain line functions	Size (nm)	Strain (%)
Cauchy/Cauchy	30 ± 20	0.9 ± 0.2
Gaussian/Gaussian	30 ± 20	1.2 ± 0.3
Cauchy/Gaussian	19 ± 3	0.9 ± 0.2

S0013-4651(99)01-103-9 CCC: $7.00

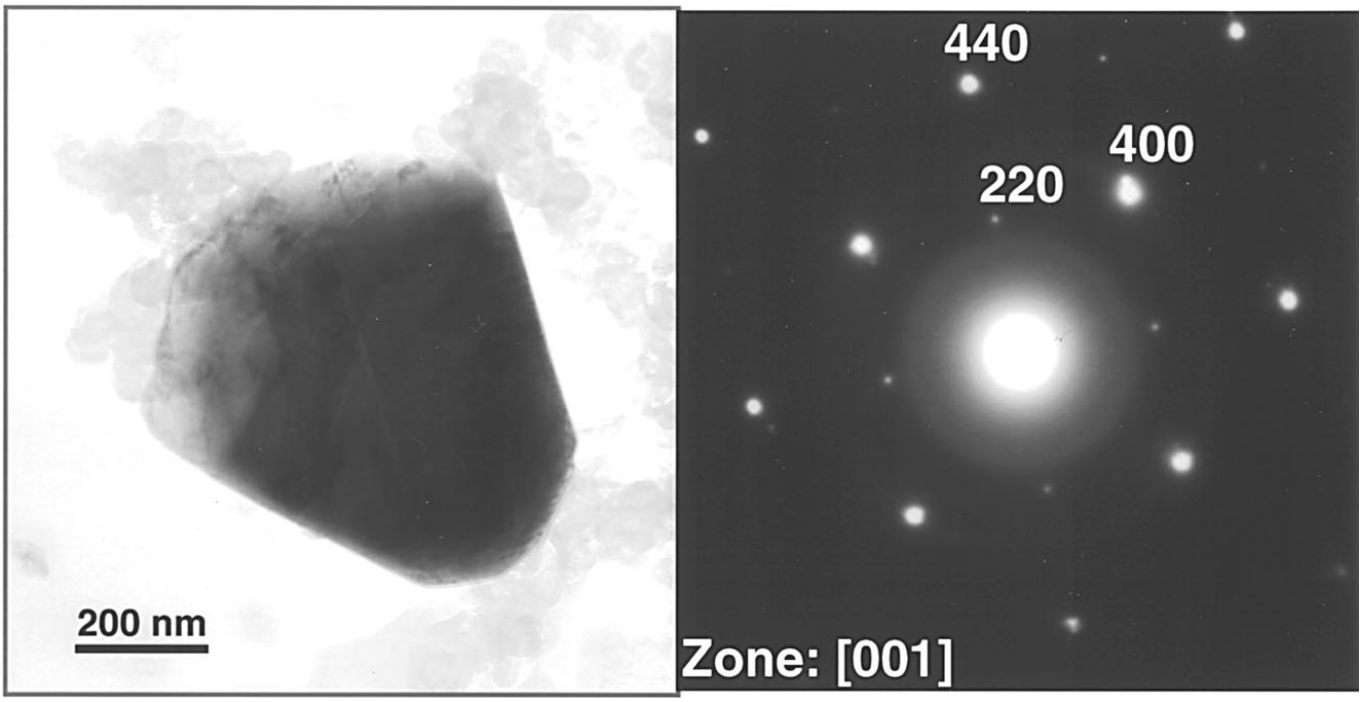

Figure 15. TEM image and corresponding SAD pattern of a single crystalline oxide particle after cycling. Electrochemical conditions are written in the text.

tent with the XRD results in Fig. 14. More precisely, the measurement error from the SAD patterns indicates a tetragonality of less than 2%. This can be contrasted with the much greater tetragonality (16%) in $Li_2Mn_2O_4$ obtained by the cycling of $LiMn_2O_4$.[30] In Fig. 15, the existence of {220} reflections is also a striking feature that is not expected in tetragonal "lithiated spinel" obtained by cycling of $LiMn_2O_4$.[30] These reflections occur only when there is tetrahedral site occupancy in the spinel,[23,26] whereas ideal $Li_2Mn_2O_4$ has only octahedral cation site occupancy.[24]

These results show that the spinel produced by electrochemical cycling of *o*-$LiMnO_2$ has a clearly distinct cation ordering compared to high-temperature synthesized $Li_xMn_2O_4$ spinel. While previous studies suggested that *o*-$LiMnO_2$ transforms to a spinel-"like" structure that is not the same as ideal $Li_xMn_2O_4$ spinel,[8-16] the details of the structural differences were not clear.

HREM observations furthermore revealed the presence of a nanodomain structure within the particles, appearing as mosaic patterns of 20 to 50 nm width with very fine strain contours. This fine scale microstructure is seen in Fig. 16. A high-resolution image of such domains is shown in Fig. 17. The boundary between two adjacent domains is marked by the facing arrows. The SAD pattern from the upper domain shows a cubic spinel structure with {220} reflections, indicating tetrahedral site occupancy, while the lower domain shows a superlattice diffraction pattern with twice the periodicity of cubic spinel. The contrast in the lattice image and the reflections in the diffraction patterns indicate that the two domains are slightly misoriented. However, many features in the two patterns are parallel, and the overall particle morphology is uninterrupted, showing that the domains originated from the same single crystal, and that overall single crystallinity is retained during the cycling-induced transformation. Other particles showed similar features.

The length scale of the nanodomain structure is in good agreement with the size broadening determined from the XRD pattern, being in the range of 20-50 nm. The strain broadening may result from an inhibited transformation to tetragonal spinel, or from Li concentration variation within the particles. The detailed structure of the superlattice domain is not yet understood. In addition to the structural differences, each domain may also have a different Li content. The widespread occurrence of nanodomains in each observed particle strongly suggests that their formation is closely related to cycling stability.

We have also observed this kind of nanodomain structure in cycled orthorhombic and monoclinic $LiAl_yMn_{1-y}O_2$.[31] In that work a mechanism was proposed by which the orthorhombic and monoclinic polymorphs of $LiMnO_2$ are able to undergo a cycling-induced transformation to spinel ordering without suffering the mechanically destructive aspects of a collective Jahn-Teller distortion. In brief, the massive reordering of Mn ions necessary to transform the crystal from the orthorhombic or monoclinic phases to spinel can occur nonuniformly within the crystal during electrochemical cycling, and is the cause of nanodomain formation. In contrast, high-temperature synthesized $LiMn_2O_4$ has perfect spinel ordering of Mn throughout

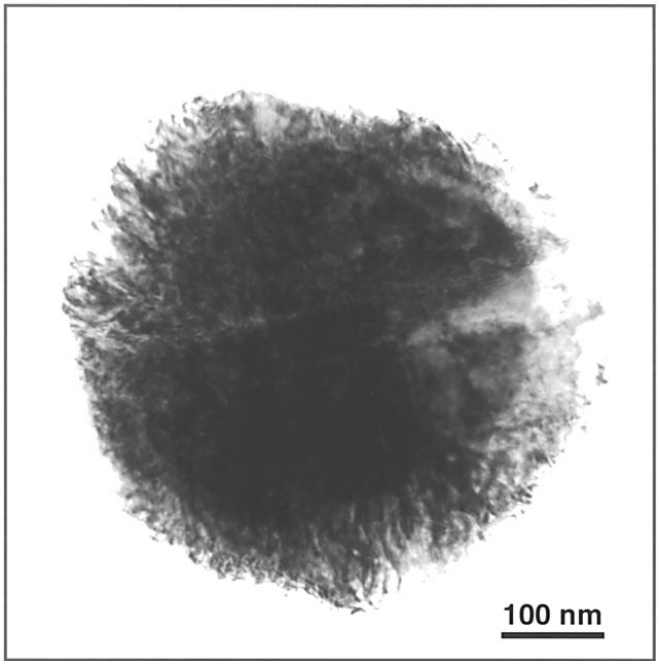

Figure 16. HREM image of a cycled oxide particle showing nanodomain structure with very fine strain contours.

S0013-4651(99)01-103-9 CCC: $7.00 © The Electrochemical Society, Inc.

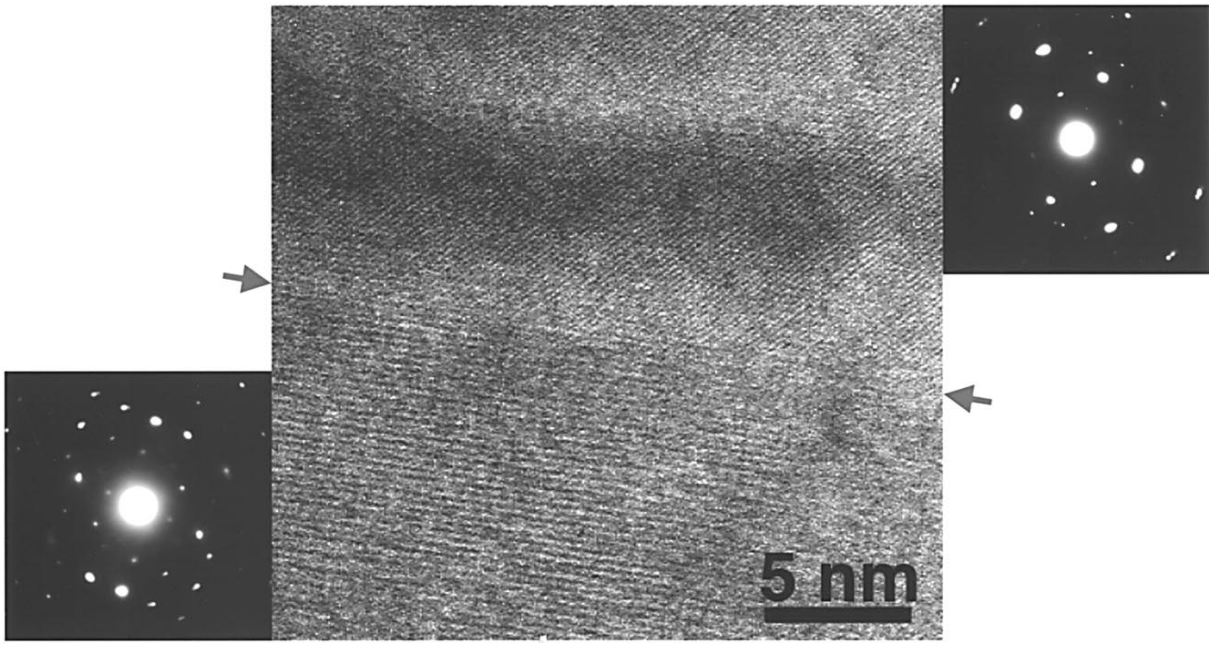

Figure 17. HREM image and corresponding SAD patterns of two adjacent nanodomains formed in a single crystalline oxide particle after cycling. The facing arrows indicate the boundary between two adjacent domains.

the crystal from the beginning, and cycling does not change this ordering. When nanodomains are present, they can differ in the relative stability of the tetragonal *vs.* cubic phase or even in the preferred direction of the Jahn-Teller distortion. Interference between nanodomains thereby prevents a collective overall distortion from propagating throughout a crystalline particle. The relatively high level of strain broadening observed in the present samples is consistent with this model. Mixing of the Mn ions among cation sites can also contribute to the suppression of the collective Jahn-Teller distortion.

Further studies using HREM are expected to clarify additional details of the structure of partially transformed materials. However, the present results clearly show that spinel produced by the electrochemical cycling of *o*-$LiMnO_2$ differs in both cation ordering and microstructure from conventional $Li_xMn_2O_4$ spinel.

Conclusions

A high-charge-capacity orthorhombic $LiMnO_2$ has been synthesized by high temperature firing of homogeneous precursors in a reduced oxygen partial pressure atmosphere. When cycled over both the 4 and 3 V plateaus, no significant capacity fade was seen up to 130 cycles, unlike conventional $Li_xMn_2O_4$ spinel, even though the characteristic electrochemical profile of the spinel was observed. During an initial transient in capacity, the 3 V capacity is larger than the 4 V capacity, indicating cation disorder in the spinel structure. X-ray diffraction and electron microscopy revealed the presence of a cubic spinel in the fully lithiated state containing tetrahedral site occupancy, and a nanodomain structure. It is proposed that the collective Jahn-Teller transformation to tetragonal spinel is suppressed by cation disorder and the formation of nanodomains differing from one another in cation ordering and/or composition within individual oxide particles. At low charge/discharge rates (3.33 mA/g) a discharge capacity of 272 mAh/g (95% of the theoretical value) and an energy density of 853 Wh/kg were obtained in this material, representing the highest values yet achieved in crystalline $LiMnO_2$.

Acknowledgments

This study has been funded by the INEEL University Research Consortium. The INEEL is managed by Lockheed Martin Idaho Technology Company for the U.S. Department of Energy, Idaho Operations Offices, under contract no. DE-AC07-94ID13223. We used instrumentation in the Shared Experimental Facilities at MIT, supported by NSF grant no. 9400334-DMR.

Massachusetts Institute of Technology assisted in meeting the publication costs of this article.

References

1. J. M. Tarascon and D. Guyomard, *J. Electrochem. Soc.*, **138**, 2864 (1991).
2. R. J. Gummow and M. M. Thackeray, *J. Electrochem. Soc.*, **141**, 1178 (1994).
3. Y. Gao and J. R. Dahn, *J. Electrochem. Soc.*, **143**, 100 (1996).
4. M. M. Thackeray, A. de Kock, M. H. Rossouw, D. Liles, R. Bittihn, and D. Hodge, *J. Electrochem. Soc.*, **139**, 363 (1992).
5. J. Barker, R. Koksbang, and M. Y. Saïdi, *Solid State Ionics*, **82**, 143 (1995).
6. R. J. Gummow, A. de Kock, and M. M. Thackeray, *Solid State Ionics*, **69**, 59 (1994).
7. Y. Xia, Y. Zhou, and M. Yoshio, *J. Electrochem. Soc.*, **144**, 2593 (1997).
8. T. Ohzuku, A. Ueda, and T. Harai, *Chem. Express*, **7**, 193 (1992).
9. J. N. Reimers, E. W. Fuller, E. Rossen, and J. R. Dahn, *J. Electrochem. Soc.*, **140**, 3396 (1993).
10. R. J. Gummow, D. C. Liles, and M. M. Thackeray, *Mater. Res. Bull.*, **28**, 1249 (1993).
11. R. J. Gummow and M. M. Thackeray, *J. Electrochem. Soc.*, **141**, 1178 (1994).
12. I. Koetschau, M. N. Richard, J. R. Dahn, J. B. Soupart, and J. C. Rousche, *J. Electrochem. Soc.*, **142**, 2906 (1995).
13. I. J. Davidson, R. S. McMillan, J. J. Murray, and J. E. Greedan, *J. Power Sources*, **54**, 232 (1995).
14. L. Croguennec, P. Deniard, R. Brec, P. Biensan, and M. Broussely, *Solid State Ionics*, **89**, 127 (1996).
15. Z. X. Shu, I. J. Davidson, R. S. McMillan, and J. J. Murray, *J. Power Sources*, **68**, 618 (1997).
16. L. Croguennec, P. Deniard, and R. Brec, *J. Electrochem. Soc.*, **144**, 3323 (1997).
17. I. M. Kötschau and J. R. Dahn, *J. Electrochem. Soc.*, **145**, 2672 (1998).
18. L. Croguennec, P. Deniard, R. Brec, and A. Lecerf, *J. Mater. Chem.*, **5**, 1919 (1995).
19. L. Croguennec, P. Deniard, R. Brec, and A. Lecerf, *J. Mater. Chem.*, **7**, 511 (1997).
20. Y.-I. Jang, H. Wang, and Y.-M. Chiang, *J. Mater. Chem.*, **8**, 2761 (1998).
21. Y.-M. Chiang, Y.-I. Jang, H. Wang, B. Huang, D. R. Sadoway, and P. Ye, *J. Electrochem. Soc.*, **145**, 887 (1998).
22. B. Huang, Y.-I. Jang, Y.-M. Chiang, and D. R. Sadoway, *J. Appl. Electrochem.*, **28**, 1365 (1998).
23. H. Wang, Y.-I. Jang, B. Huang, D. R. Sadoway, and Y.-M. Chiang, *J. Electrochem. Soc.*, **146**, 473 (1999).
24. M. M. Thackeray, *Prog. Solid State Chem.*, **25**, 1 (1997).
25. T. Ohzuku, M. Kitagawa, and T. Hirai, *J. Electrochem. Soc.*, **137**, 769 (1990).
26. J. M. Tarascon, E. Wang, F. K. Shokoohi, W. R. McKinnon, and S. Colson, *J. Electrochem. Soc.*, **138**, 2859 (1991).
27. W. I. F. David, J. B. Goodenough, M. M. Thackeray, and M. G. S. R. Thomas, *Rev. Chim. Min.*, **20**, 636 (1983).
28. W. Tang, H. Kanoh, and K. Ooi, *J. Solid State Chem.*, **142**, 19 (1999).
29. H. P. Klug and L. E. Alexander, *X-Ray Diffraction Procedures: For Polycrystalline and Amorphous Materials*, p. 661, John Wiley & Sons, New York (1974).
30. M. M. Thackeray, Y. Shao-Horn, A. J. Kahaian, K. D. Kepler, E. Skinner, J. T. Vaughey, and S. A. Hackney, *Electrochem. Solid-State Lett.*, **1**, 7 (1998).
31. H. Wang, Y.-I. Jang, and Y.-M. Chiang, *Mater. Res. Soc. Symp. Proc.*, **548**, (1999), In press.